

## Synthesis of organic–inorganic hybrids by miniemulsion polymerization and their application for electrochemical energy storage†

Zichao Yang, Jingguo Shen, N. Jayaprakash and Lynden A. Archer\*

Received 19th November 2011, Accepted 20th February 2012

DOI: 10.1039/c2ee03230a

A general method is reported for creating functional organic–inorganic hybrid materials by copolymerization of organic molecules and inorganic compounds. The approach is based on a miniemulsion polymerization technique followed by a thermal pyrolysis step, and yields nanostructured composites in which nanoparticles are uniformly embedded in a porous, partially graphitic carbon matrix. The method builds upon our previous report disclosing synthesis of organic–inorganic hybrids using miniemulsion polymerization and demonstrates that *ex situ* engineering of the inorganic phase leads to remarkably improved function. We specifically show that depending upon the chemistry of the starting materials, nanoscale organic–inorganic hybrid materials created using the approach are attractive as anodes and cathodes for next-generation lithium and other rechargeable battery systems. Additionally, we show that the platform is very versatile and through *ex situ* conversion or utilization of multiple precursors, can be applied to various classes of materials including metal oxides, metals, metal sulfides and alloys. The approach also lends itself to the development of scalable processes for production of nanostructured battery materials.

### Introduction

Rising energy prices and unmet demand for secondary batteries with higher energy & power densities, higher operating voltages, improved cycling stability, enhanced safety, and lower initial and life cycle costs has increased interest in lithium ion batteries (LIB). A crucial performance criterion is the cyclability of the electrode materials and a key issue in capacity retention lies in the large structural and morphological changes many electrode materials undergo during cyclic insertion and deinsertion of

lithium.<sup>1–9</sup> Significantly, these changes occur in materials following rather different lithiation mechanisms, including alloying, conversion, and intercalation; implying that general solutions are required. Creating lower dimensional nanostructures serves as a means to mitigate the problem through shortening lithium diffusion paths and reducing mechanical strains during cycling, but usually further enhancements are still required.<sup>7,10–15</sup>

A commonly used strategy is to create nanocomposites containing the active material, among which carbon composites have been a popular choice<sup>16–22</sup> because of the low cost of carbon and the ease of synthesis. Common methods of synthesizing carbon nanocomposites typically involve post treatment of the active particles after synthesis with a precursor that upon pyrolysis yields carbon, or combining the preformed particles with

School of Chemical and Biomolecular Engineering, Cornell University, Ithaca, New York 14853, USA. E-mail: laa25@cornell.edu

† Electronic supplementary information (ESI) available. See DOI: 10.1039/c2ee03230a

### Broader context

New materials that can handle the physical and chemical stresses associated with repeated insertion and de-insertion of lithium present a fundamental challenge to further development of next-generation lithium ion battery (LIB) technologies that offer higher energy storage capacity, higher power, and more stable performance. In many of the most promising LIB electrode materials (*e.g.* Sn, Si, and many transition metal oxides), these stresses typically lead to mechanical failure and undesirable chemical changes in secondary batteries, which causes reduction in their energy storage capacity over time (capacity fade). Significantly, the problem exists in LIB electrodes that rely on all known electrochemical storage mechanisms (alloying, conversion reaction, and intercalation). In this work, we report a general approach for synthesizing metal oxide–, metal sulfide–, and metal alloy–carbon nanocomposites designed to ameliorate these stresses. Remarkably, in every case investigated the nanocomposites manifest improved electrochemical stability whether they are applied as anodes or cathodes in a secondary battery.

a preformed conductive carbon material (e.g. graphene/CNT).<sup>23,24</sup> The enhancement in electrochemical performance observed is usually attributed to the beneficial and sometimes synergistic effects of mechanical buffering, which allows the active material structures to withstand larger stresses during lithiation/delithiation and improvement of the overall electrical conductivity of the electrode.

Herein we report an approach for the *in situ* synthesis of nanoparticles embedded in a carbon matrix through a mini-emulsion polymerization technique. We further show that the as-prepared carbon-nanoparticle hybrid materials can be facily modified *ex situ* to significantly increase the range of materials chemistries that can be achieved by the method. The approach is based on the *in situ* synthesis of inorganic nanoparticles and organic polymers from precursors capable of forming chemical cross-links with each other.<sup>25</sup> After pyrolysis of the organic phase, the process yields a well-defined nanostructured material comprised of discrete inorganic nanoparticles embedded in a porous carbon matrix. Post treatment of the embedded particles creates carbon-nanoparticle hybrids based on metals, metal alloys, and a variety of other particles attractive for lithium battery applications.

Emulsion polymerization is a widely used method for synthesizing polymer latexes for applications such as adhesives and coatings. The method typically uses monomers with low water solubility, stabilized by surfactant in an aqueous media. The polymerization rate is limited by the diffusion of reactive monomer, through the aqueous phase, from monomer droplets to monomer-swollen polymer particles where polymerization takes place. Application of high shear force to the emulsion yields a so-called miniemulsion, comprised of droplets with small sizes, usually 0.01–0.5  $\mu\text{m}$ , compared to 1–10  $\mu\text{m}$  in conventional emulsion polymerization. Because of the high surface area of monomer droplets in a miniemulsion, nucleation takes place mainly *via* radical entry into the emulsified monomer droplets and reaction proceeds through polymerization of the monomers in these small droplets.<sup>26</sup> If more than one monomer chemistry is employed simultaneously or sequentially, the approach can be used to create copolymers with different architectures.<sup>27,28</sup> If the polymerization reaction is performed in the presence of guest species miscible with the monomer (e.g. dyes, metal complexes, *etc.*), the guest species can be embedded in the polymer particle host.<sup>29</sup> However, a common drawback is that only relatively low loadings (a few percent by weight) of the guest can be achieved.<sup>30</sup> Here we report a new method to overcome this drawback and demonstrate the applicability of the method to synthesize composites involving various types of LIB electrode materials.

## Experimental procedure

### Chemicals and materials synthesis

Chemical reagents were purchased from Sigma-Aldrich and used without purification.  $\text{Fe}_3\text{O}_4/\text{C}$  nanocomposite was synthesized according to a previously reported procedure.<sup>25</sup> 2 ml acrylonitrile (AN), 2 ml divinylbenzene (DVB) and 2 g of iron undecylenate were mixed to form a homogeneous solution. 3 mg of azobisisobutyronitrile (AIBN) and 100 mg sodium dodecyl sulfate (SDS) were added to 25 ml of water and the former solution

added dropwise to the aqueous phase under sonication with a Sonics VCX500 horn (500 W, 20 kHz, amplitude 50%). The mixture was sonicated for 3 min and after a stable emulsion was formed, heated at 70 °C for 12 h. Sodium chloride was added to induce aggregation of the resultant polymer–inorganic hybrid particles, which were collected by centrifugation. The material obtained was heated in an argon atmosphere, first to 320 °C, held at this temperature for 1 h, then to 500 °C and held for 2 h to obtain the  $\text{Fe}_3\text{O}_4/\text{C}$  nanocomposite product.  $\text{Fe}_3\text{O}_4/\text{C}$  was then ground into powder and heated at 650 °C in a tube furnace under a 7%  $\text{H}_2$  (balance Ar) gas environment for 2 h to obtain  $\text{Fe}/\text{C}$  powders. The latter is mixed with  $2 \times$  mass of sulfur, loaded into a Pyrex tube, sealed and heated at 500 °C for 4 h to obtain  $\text{FeS}_2/\text{C}$  nanocomposite. The product is washed with  $\text{CS}_2$  to remove any residual elemental sulfur. To synthesize  $\gamma\text{-Fe}_2\text{O}_3/\text{C}$  and  $\alpha\text{-Fe}_2\text{O}_3/\text{C}$  composites,  $\text{Fe}_3\text{O}_4/\text{C}$  powder is heated in air at 350 °C for 5 h and 390 °C for 1 h, respectively, to obtain the products. To synthesize  $\text{V}_2\text{O}_5/\text{C}$ ,  $\text{VCl}_3$  is used as the starting material to synthesize  $\text{V}(\text{C}_{10}\text{H}_{19}\text{COO})_3$ . After polymerizing with acrylonitrile, the material is pyrolyzed at 500 °C in argon for 2 h and then heated in air at 390 °C for 1 h to obtain  $\text{V}_2\text{O}_5/\text{C}$ . To synthesize  $\text{FeSn}_2/\text{C}$  nanocomposite, tin undecylenate ( $\text{Sn}(\text{C}_{10}\text{H}_{19}\text{COO})_2$ ) was synthesized in a similar fashion as iron undecylenate, except with  $\text{SnCl}_2$  as the starting material. 2.2g  $\text{Fe}(\text{C}_{10}\text{H}_{19}\text{COO})_3$  and 1.8 g  $\text{Sn}(\text{C}_{10}\text{H}_{19}\text{COO})_2$  were mixed first, 2 ml AN and 2 ml DVB were added, and then the rest of the procedure was carried out as above.

### Characterization

The crystal structures of the particles were characterized using Scintag Theta-theta PAD-X X-Ray Diffractometer ( $\text{Cu-K}\alpha$ ,  $\lambda = 1.5406 \text{ \AA}$ ) and their morphologies were studied using FEI Tecnai G2 T12 Spirit Transmission Electron Microscope (120kV). Thermogravimetric analysis was performed using TA Instruments Q5000 IR Thermogravimetric Analyzer. Mercury porosimetry was performed with a Micromeritics AutoPore IV 9500 mercury porosimeter.

### Cell assembly and testing

Electrochemical characterization of the composites as anode materials in rechargeable lithium-ion batteries was performed at room temperature in 2032 coin-type cells. The working electrode consisted of 80 wt% of the active material, 10 wt% of carbon black (Super-P Li from TIMCAL) as a conductivity aid, and 10 wt% of polymer binder (PVDF, polyvinylidene fluoride, Aldrich). Copper foil was used as the current collector for nanocomposites targeted for application as the LIB anode and aluminum for those targeted as cathodes. Lithium foil was used as the counter and reference electrode for evaluating both the anode and cathode materials. A 1 M solution of  $\text{LiPF}_6$  in a 50 : 50 w/w mixture of ethylene carbonate and dimethyl carbonate was used as the electrolyte. Celgard 2500 polypropylene membranes are used as the separator. Assembly of cell was performed in a glove box with moisture and oxygen concentrations below 0.1 ppm. The room-temperature electrode capacities were measured using Neware CT-3008 battery testers. Cyclic voltammetry was performed with a CHI600D potentiostat.

## Results and discussion

Scheme 1 illustrates the chemistry of a miniemulsion polymerization methodology that could be used to create organic–inorganic hybrid copolymers with high inorganic loadings. Using an organic monomer (*e.g.* acrylonitrile, or AN) and the metal salt of an unsaturated carboxylic acid (*e.g.* iron(III) undecylenate) and divinylbenzene as crosslinker the method yields well-defined iron oxide nanoparticles uniformly embedded in a polyacrylonitrile host (Fig. 1 A). FTIR spectra of iron(III) undecylenate and the AN-iron copolymer composite are compared in Fig S1. Significant decrease in the intensity of the C=C stretch peak at around  $1640\text{ cm}^{-1}$  (normalized with respect to C–H stretch at around  $2910\text{ cm}^{-1}$ ) is observed, showing that as expected many of the double bonds in iron(III) undecylenate have been eliminated during polymerization.

We reported previously, that upon thermal treatment, the as-prepared polyacrylonitrile (PAN) – nanoparticle hybrids are transformed into carbon- $\text{Fe}_3\text{O}_4$  nanocomposites characterized by the uniform distribution of  $\text{Fe}_3\text{O}_4$  in a partially graphitic carbon host. When evaluated as the anode in a lithium ion battery, the material showed significantly improved cycling stability<sup>25</sup> and capacity retention relative to anodes based on pristine  $\text{Fe}_3\text{O}_4$  nanoparticles. The performance enhancement brought about by the *in situ* synthesis approach was argued to largely originate from the uniform separation of the embedded nanoparticles achieved in the composites, which simultaneously minimizes aggregation of the active nanostructures, facilitates electron transport, and maximizes the degree to which the carbon framework is able to absorb and isolate mechanical stresses produced by structural changes. Fig. 1B shows the TEM image of the nanocomposite after 100 charge–discharge cycles. It indicates that with the mechanical support provided by the carbon matrix, the pulverization of the active material nanoparticles is mitigated, which we believe is the source of the observed improvement in cyclability.

A goal of the present work is to illustrate the versatility of the synthesis method and to evaluate the generality of the hybrids produced. Scheme 2 shows an abbreviated list that identifies the variety of hybrid materials relevant for application in lithium

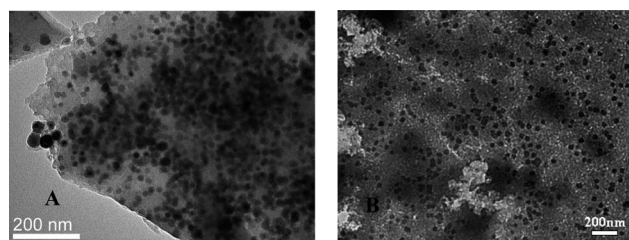
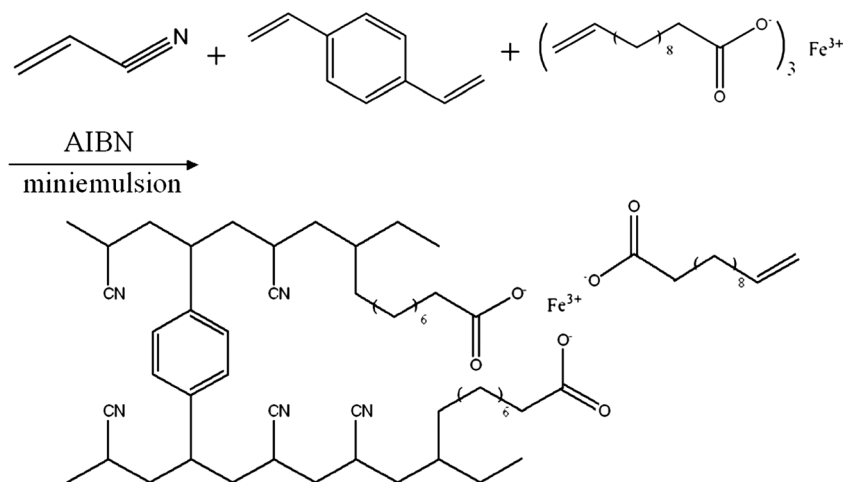


**Fig. 1** TEM images of  $\text{Fe}_3\text{O}_4@\text{C}$  nanocomposite (A) before cycling and (B) after 100 charge–discharge cycles.

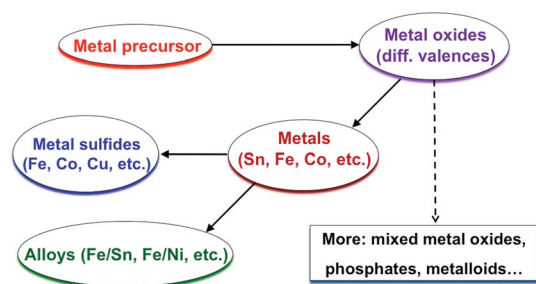
battery electrodes that can be synthesized using the approach. Because of the large number of Fe-based compounds and alloys that are of interest for LIB applications, we here demonstrate the simplicity and versatility of the method using nanoparticles based on Fe compounds; we subsequently evaluate the enhancements in properties by using the composites as anodes or cathodes for LIBs. Results on other examples (*e.g.* materials based on vanadium and titanium) will also be discussed.

As illustrated in Scheme 2, carbon- $\text{Fe}_3\text{O}_4$  nanocomposites ( $\text{Fe}_3\text{O}_4@\text{C}$ ) synthesized using the procedures outlined earlier can be reduced to  $\text{Fe}@\text{C}$  composites either by heating the material in an  $\text{H}_2$  environment or simply by heating the composite in an inert gas to a temperature somewhat higher than the carbonization temperature (whereby carbon serves as the reducing agent). The powder XRD pattern of the material obtained after heating  $\text{Fe}_3\text{O}_4@\text{C}$  to  $650\text{ }^\circ\text{C}$  under  $\text{H}_2$  is shown in Fig. 2A, which is unambiguously assigned to the  $\alpha\text{-Fe}$  phase (JCPDS card #06-0696). Fig. 2B is a transmission electron micrograph of the material showing that the materials are comprised of well-dispersed *ca* 30 nm Fe nanoparticles, which is consistent with the average crystallite size of 29 nm deduced from XRD.

Because the carbon matrix is porous, it allows the infusion of other chemical agents, which can react with the embedded Fe nanoparticles.  $\text{FeS}_2$  is a promising cathode material for lithium batteries because of its high reversible capacity ( $625\text{ mAh/g}$ ), low cost and low toxicity. It is well-known in primary lithium battery applications and high temperature thermal batteries, but its use in room-temperature rechargeable cells has been hindered by the



**Scheme 1** Schematic of synthesis process for creating organic–inorganic copolymer hybrids.

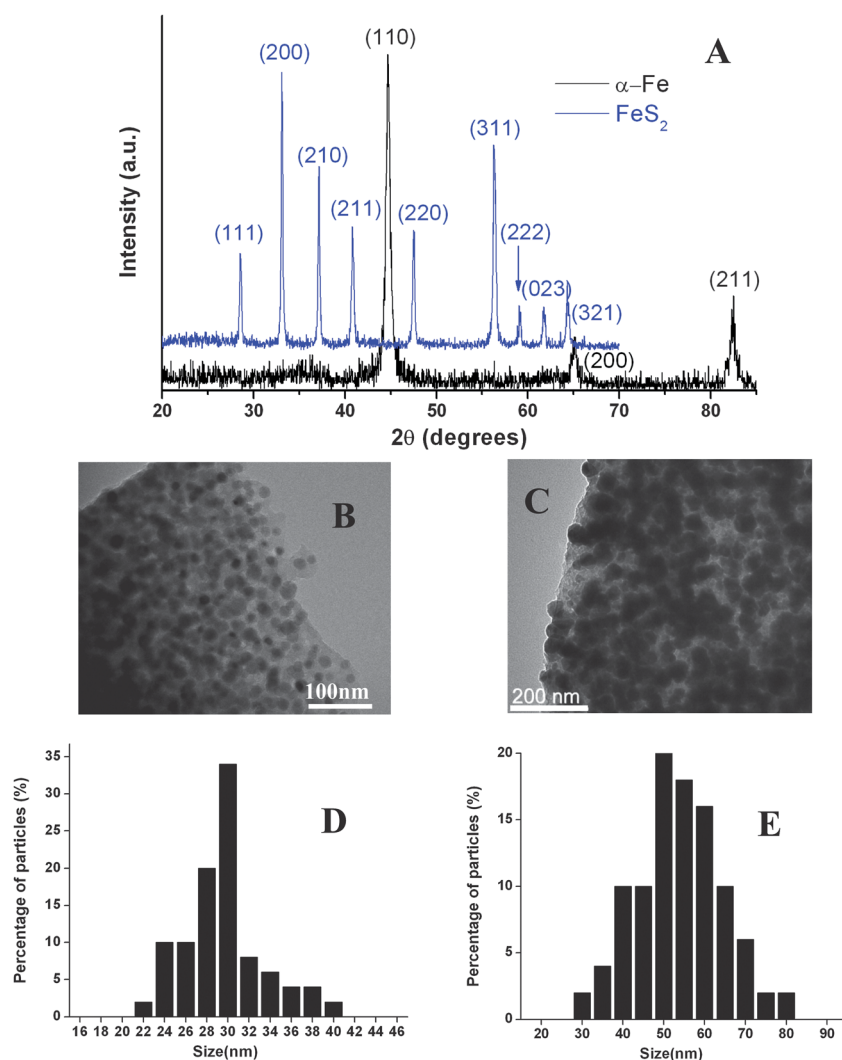


**Scheme 2** Overview of the platform for synthesizing nanocomposites with embedded structures involving different classes of materials.

material's limited cyclability.<sup>31–35</sup> The vapor infusion procedure reported previously,<sup>36</sup> was used to react the Fe@C composites with sulfur at 500 °C. Fig. 2A and C show the XRD and TEM image for the product. The XRD pattern is unambiguously assigned to FeS<sub>2</sub> (pyrite JCPDS card # 42-1340) and reveals that reaction with sulfur has nearly doubled the crystallite size to

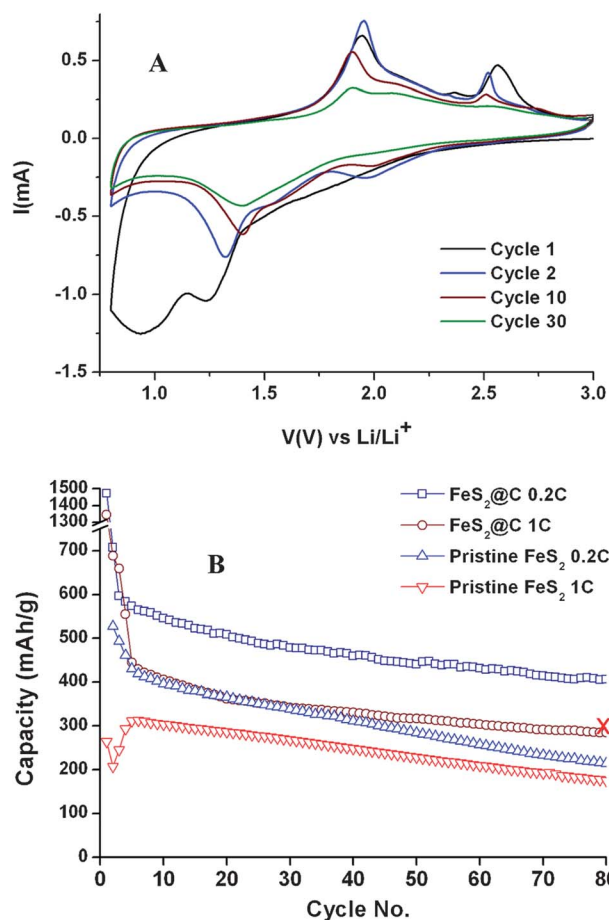
54 nm; again consistent with results from TEM, which show uniformly distributed *ca* 55 nm FeS<sub>2</sub> particles in the carbon host. Particle size histograms obtained from TEM images for Fe@C and FeS<sub>2</sub>@C composites are shown in Fig. 2(D) and (E), with average sizes of  $29.7 \pm 3.8$  nm and  $53.8 \pm 9.9$  nm, respectively. Through oxidative TGA (Fig. S2†) the weight fraction of FeS<sub>2</sub> in the product is found to be 75%.

Fig. 3 report results from cyclic voltammetry and galvanostatic cycling measurements performed using the as prepared FeS<sub>2</sub>@C composites. In the cathodic scan of the first cycle, FeS<sub>2</sub> follows a two-step lithiation:  $\text{FeS}_2 + 2\text{Li}^+ + 2\text{e}^- \rightarrow \text{Li}_2\text{FeS}_2$  ( $\sim 2$  V) and  $\text{Li}_2\text{FeS}_2 + 2\text{Li}^+ + 2\text{e}^- \rightarrow \text{Fe} + 2\text{Li}_2\text{S}$  ( $\sim 1.4$  V). In the anodic scans, the material is converted to Li<sub>2</sub>FeS<sub>2</sub> at around 1.8 V and then to Li<sub>2-x</sub>FeS<sub>2</sub> ( $0 < x < 0.8$ ) at around 2.5 V.<sup>34</sup> At room temperature if the material is driven to high potentials (above 2.45 V), instead of regenerating the FeS<sub>2</sub> (cubic structure), FeS<sub>x</sub> and elemental sulfur may be formed because of the relative ease of transformation from Li<sub>2-x</sub>FeS<sub>2</sub> (hexagonal) to FeS<sub>x</sub> (hexagonal). Subsequent cycling occurs between Li<sub>2-x</sub>FeS<sub>2</sub> and Fe/Li<sub>2</sub>S. Voltage–capacity profiles at different charging rates are



**Fig. 2** Powder XRD patterns (A), TEM images for Fe@C (B) and FeS<sub>2</sub>@C (C) composites and size distribution histograms for Fe@C (D) and FeS<sub>2</sub>@C (E).





**Fig. 3** (A) Cyclic voltammograms of FeS<sub>2</sub>@C; (B) cycling performance of FeS<sub>2</sub>@C and pristine FeS<sub>2</sub>. Red cross indicates result from ref. 28 (0.58C).

shown in Fig. S3.† Plateaus at ~2 V and 1.4–1.5 V in the discharge curve correspond to lithiation peaks in the anodic scan. The gravimetric capacity is calculated with respect to active

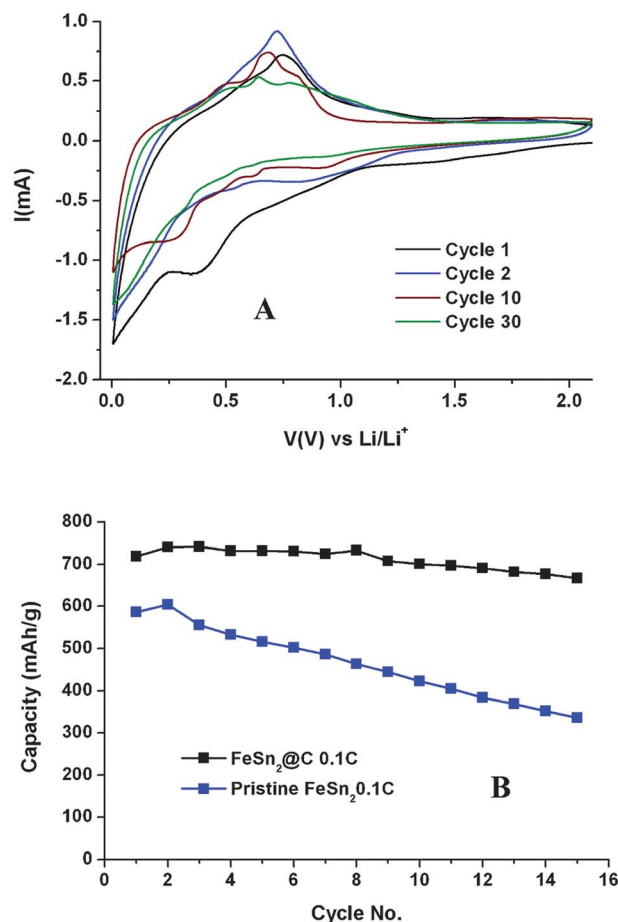


**Fig. 5** (A) Cyclic voltammograms of FeSn<sub>2</sub>@C; (B) cycling performance of FeSn<sub>2</sub>@C and pristine FeSn<sub>2</sub> at 0.1 C.

material mass (the same for the materials to follow in this work). The cyclability is compared with commercially available pristine FeS<sub>2</sub> and with results reported in ref. 28 (Huang *et al.*, 0.58 C),

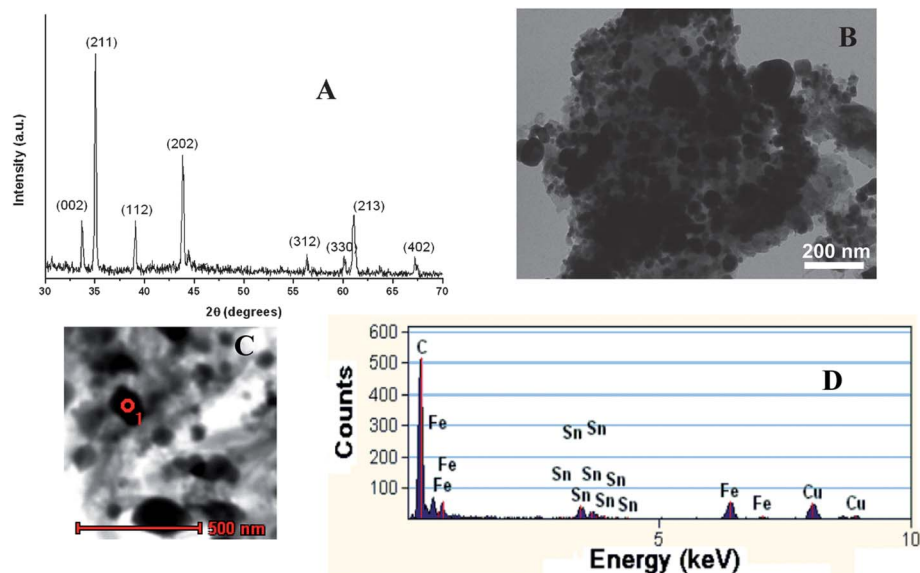


**Fig. 4** (A) XRD pattern, (B) TEM image, (C) STEM image and (D) EDX spectrum for FeSn<sub>2</sub>@C nanocomposite.

showing the enhancement of cycling performance brought about by forming nanocomposites with carbon.

When more than one metal precursor is used, the approach may yield nanocomposites consisting of alloy nanoparticles embedded in the carbon matrix. An example of this is the iron–tin alloy, which is being actively investigated as an anode material in LIBs. Alloys of tin with another metal (*e.g.* Sb, Co, Fe, Ni) have been studied as materials which are able to provide some alleviation effect for the pulverization of tin through the mechanical protection offered by the other metal which gets extruded during lithiation.<sup>37–43</sup> The incorporation of such alloy nanoparticles in a carbon matrix provides a means of additional mechanical support so that the cycling stability of the material may be further enhanced.

FeSn<sub>2</sub>@C nanocomposites can be synthesized using a combination of iron and tin precursors, as confirmed by XRD (Fig. 4A). EDX indicates the presence of iron and tin in the composite (Fig. 4C and 4D) and yields an atomic ratio of Fe/Sn = 0.59. The weight fraction of FeSn<sub>2</sub> in the composite is determined using oxidative TGA to be 68% (Fig. S2†). The TEM images are shown in Fig. 4B. There appears to be a broader

distribution of nanoparticle size compared to other materials (*e.g.* metal oxides, sulfides) synthesized using the same approach. The reason may be that tin has a relatively low melting point and liquid tin likely formed droplets with broad size distribution before reacting with iron. Cyclic voltammograms of the material are shown in Fig. 5A. The electrochemical reaction of FeSn<sub>2</sub> in LIB can be expressed as follows:  $\text{FeSn}_2 + 8.8\text{Li}^+ + 8.8\text{e}^- \rightarrow 2\text{Li}_{4.4}\text{Sn} + \text{Fe}$  and  $\text{Li}_{4.4}\text{Sn} \rightarrow \text{Sn} + 4.4\text{Li}^+ + 4.4\text{e}^-$ .<sup>44</sup> The reversible capacity of the material results from the repeated alloying and dealloying of lithium with tin. Multiple lithiation peaks occur in the CV indicating the multi-step reaction associated with Li–Sn alloying. Some of the important intermediate phases include Li<sub>7</sub>Sn<sub>3</sub> (formed at ~0.45V vs. Li/Li<sup>+</sup>) and Li<sub>7</sub>Sn<sub>2</sub> (~0.28 V).<sup>45</sup> Overlapping with the SEI formation peak may have caused some broadening of these lithiation peaks. The cycling performance of the composite at different rates is compared with pristine FeSn<sub>2</sub> synthesized from heating a mixture of iron and tin powders at 500 °C and enhancement over the bare material is clearly seen.

*Ex situ* treatment may also be performed on metal oxides themselves to yield the oxides with different valences of the metal. This brings about a method to overcome the limitations

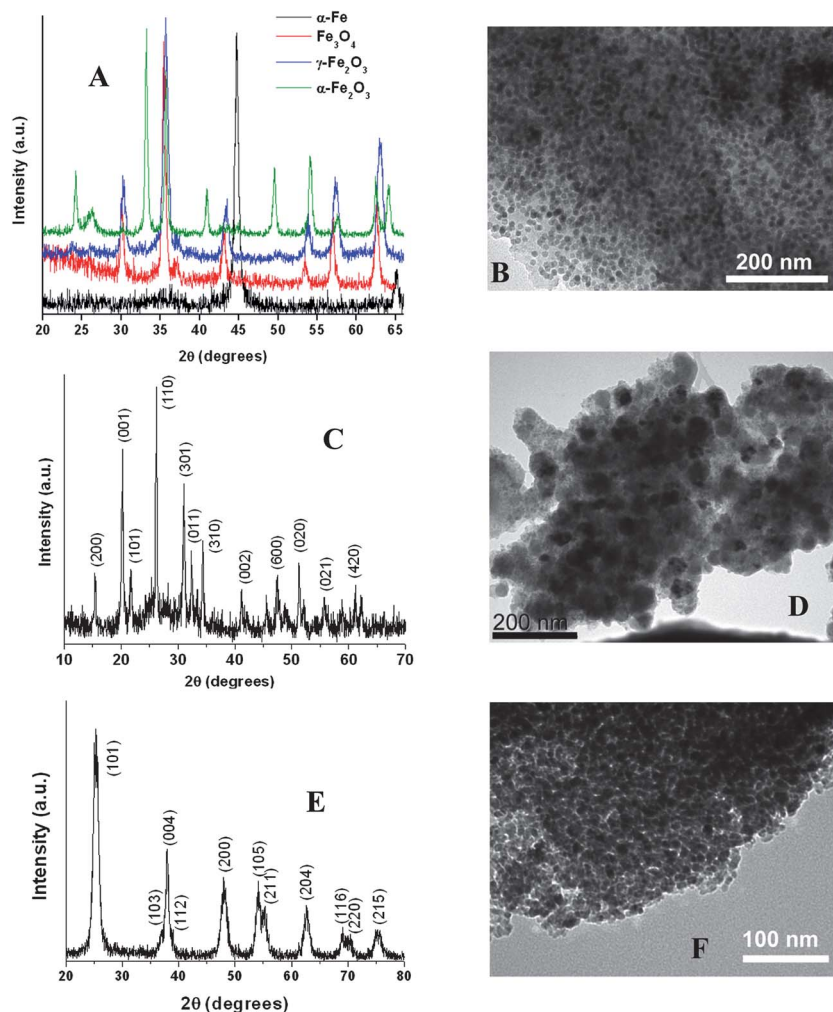


**Fig. 6** (A) XRD patterns of the embedded carbon composites involving iron/iron oxides; (B) TEM image of  $\gamma\text{-Fe}_2\text{O}_3$ @C composite; (C) and (D) XRD pattern and TEM image of  $\text{V}_2\text{O}_5$ @C composite; (E) and (F) XRD pattern and TEM image of  $\text{TiO}_2$ @C composite.

on the types of metal oxides that can be synthesized using the current approach. There are two main reasons for this limitation. One is that in general metal salts with higher valences has a higher tendency to hydrolyze and the corresponding carboxylic acid salt may be more difficult to synthesize. For example, only  $\text{Mn}(\text{C}_{10}\text{H}_{19}\text{COO})_2$  can be synthesized using the current approach and not  $\text{Mn}(\text{C}_{10}\text{H}_{19}\text{COO})_3$ . The other is that with a given precursor, usually only one type of metal oxide can be obtained from the direct pyrolysis of the precursor. For example, the pyrolysis of the  $\text{Fe}(\text{C}_{10}\text{H}_{19}\text{COO})_3$  precursor only yields magnetite and does not directly give maghemite or hematite. With *ex situ* oxidation, the composites involving lower-valence metal oxides may be transformed into composites containing metal oxides with higher valences, which cannot be directly made. For example,  $\text{Fe}_3\text{O}_4$  (magnetite) may be oxidized to maghemite or hematite and  $\text{MnO}$  may be oxidized to form  $\text{Mn}_2\text{O}_3$ . The XRD patterns of  $\alpha\text{-Fe@C}$  (JCPDS card #06-0696),  $\text{Fe}_3\text{O}_4\text{@C}$  (#19-0629),  $\alpha\text{-Fe}_2\text{O}_3\text{@C}$  (#33-0664) and  $\gamma\text{-Fe}_2\text{O}_3\text{@C}$  (#25-1402) are shown in Fig. 6A and TEM image for  $\gamma\text{-Fe}_2\text{O}_3\text{@C}$  in 6B.

Another example is vanadium.  $\text{V}(\text{v})$  salt is not stable in water and  $\text{V}_2\text{O}_5$  cannot be directly synthesized using this approach. However,  $\text{V}(\text{m})$  salt may be used to synthesize  $\text{V}(\text{C}_{10}\text{H}_{19}\text{COO})_3$  precursor which can be pyrolyzed to form  $\text{VO}_2\text{@C}$  which is then oxidized in air to give  $\text{V}_2\text{O}_5\text{@C}$  composite. The XRD patterns and TEM images of  $\text{V}_2\text{O}_5\text{@C}$  (JCPDS card #41-1426) and  $\text{TiO}_2\text{@C}$  (anatase, JCPDS card #21-1272) are shown in Fig. 6C–F.

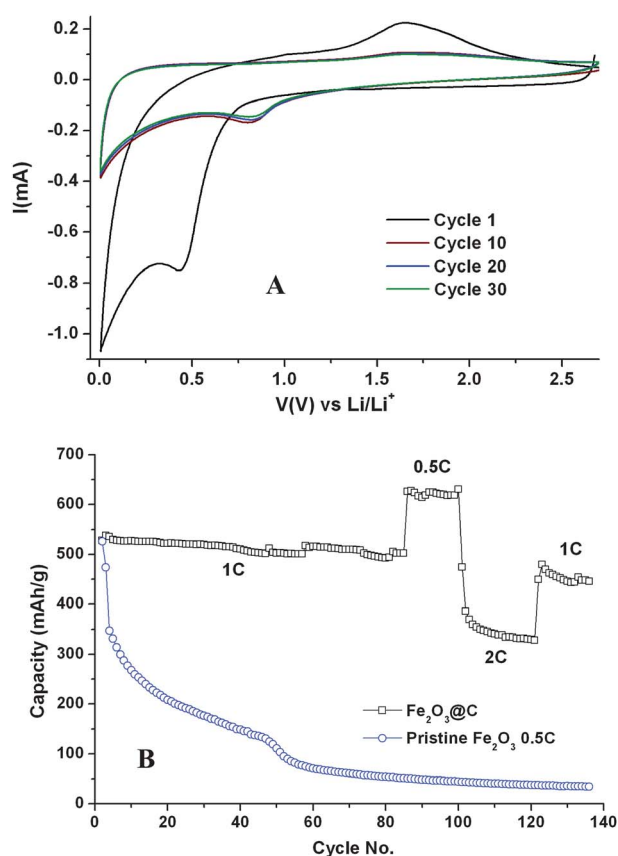


**Fig. 7** (A) Cyclic voltammograms of  $\gamma\text{-Fe}_2\text{O}_3\text{@C}$ ; (B) cycling performance of  $\gamma\text{-Fe}_2\text{O}_3\text{@C}$  at 0.5 C, 1 C and 2 C and pristine  $\text{Fe}_2\text{O}_3$  at 0.5 C.

The electrochemical performance of  $\gamma\text{-Fe}_2\text{O}_3\text{@C}$  was tested.  $\alpha\text{-Fe}_2\text{O}_3$  has been extensively investigated as LIB electrode materials undergoing either intercalation mechanism at low levels of lithiation or conversion reaction at high levels of lithiation<sup>2,46–49</sup> and there have also been some reports on  $\gamma\text{-Fe}_2\text{O}_3$ .<sup>48,50</sup> Cyclic voltammograms of the  $\gamma\text{-Fe}_2\text{O}_3\text{@C}$  composite synthesized using the current method are shown in Fig. 7A.  $\text{Fe}_2\text{O}_3$  nanoparticles follow the reversible conversion reaction  $\text{Fe}_2\text{O}_3 + 6\text{Li}^+ + 6\text{e}^- \leftrightarrow 2\text{Fe} + 3\text{Li}_2\text{O}$  when fully lithiated. The large peak in the first cathodic scan at  $\sim 0.5$  V vs.  $\text{Li}/\text{Li}^+$  is usually attributed to SEI formation and in the subsequent cycles lithiation of  $\text{Fe}_2\text{O}_3$  takes place at  $\sim 0.8$  V corresponding to the reduction of  $\text{Fe}^{3+}$  to  $\text{Fe}^0$ . The broad peak centered at  $\sim 1.7$  V in the anodic scan corresponds to the reoxidation of  $\text{Fe}^0$  to  $\text{Fe}^{3+}$ . The overlapping of the traces of cyclic voltammograms indicates stable cycling performance, which is shown in Fig. 7B at 1 C, 0.5 C and 2 C charging rates.

Since the active material is incorporated in an amorphous carbon matrix, which does not make a significant contribution to the lithiation capacity, it is useful to determine the effect of the carbon. Using as an example the  $\text{Fe}_3\text{O}_4$ -carbon nanocomposite containing 66% by weight  $\text{Fe}_3\text{O}_4$  (924 mAh/g) and the balance carbon (40 mAh/g),<sup>25</sup> the gravimetric theoretical capacity of the composite is 620 mAh/g. From mercury porosimetry, the pore volume of carbon is found to be  $0.5516 \text{ mL g}^{-1}$  and assuming the bulk densities of magnetite and amorphous carbon to be 5.2 and  $2.1 \text{ g cm}^{-3}$ , respectively, the volumetric theoretical capacities of magnetite and the composite are 4.81 and  $1.30 \text{ Ah cm}^{-3}$ . Therefore the employment of the porous carbon matrix comes at the cost of a reduced volumetric capacity, which can be limited in an actual battery design by engineering the porosity and weight fraction of the carbon matrix to achieve desired gravimetric and volumetric capacity goals while preserving the improving cyclability imparted by the porous carbon support.

## Conclusion

In conclusion, a platform has been developed whereby through the copolymerization of organic and inorganic starting materials and formation of a hybrid followed by calcination, embedded nanostructures consisting of uniformly sized nanoparticles incorporated in a porous carbon matrix may be synthesized *in situ*. Either by mere *in situ* reaction, or combined with *ex situ* engineering of the embedded material, a wide variety of embedded nanostructures may be synthesized which show enhanced lithium storage performance over the bare material. The method obviates the relatively stringent experimental control required in many other methods of creating carbon composites and provides a convenient way to prevent the aggregation of particles. Therefore the process lends itself to cheap and facile scale-up. Besides the materials, which have been demonstrated, additional categories of materials can be made using the current approach (*e.g.* silicon and phosphates), which is part of the ongoing work.

## Acknowledgements

This material is based on work supported as part of the Energy Materials Center at Cornell, an Energy Frontier Research Center

funded by the U.S. Department of Energy, Office of Science, Office of Basic Energy Sciences under Award Number DE-SC0001086. Cornell Center for Materials Research is acknowledged for use of facilities. The authors also thank Don-Hyung Ha for assistance with EDX characterization.

## References

- 1 P. Poizot, S. Laruelle, S. Grugeon, L. Dupont and J. M. Tarascon, *Nature*, 2000, **407**, 496.
- 2 J. Chen, L. N. Xu, W. Y. Li and X. L. Gou, *Adv. Mater.*, 2005, **17**, 582.
- 3 D. V. Bavykin, J. M. Friedrich and F. C. Walsh, *Adv. Mater.*, 2006, **18**, 2807.
- 4 J. Cabana, L. Monconduit, D. Larcher and M. R. Palacin, *Adv. Mater.*, 2010, **22**, E170.
- 5 K. T. Lee, Y. S. Jung and S. M. Oh, *J. Am. Chem. Soc.*, 2003, **125**, 5652.
- 6 W. M. Zhang, J. S. Hu, Y. G. Guo, S. F. Zheng, L. S. Zhong, W. G. Song and L. J. Wan, *Adv. Mater.*, 2008, **20**, 1160.
- 7 C. K. Chan, H. L. Peng, G. Liu, K. McIlwrath, X. F. Zhang, R. A. Huggins and Y. Cui, *Nat. Nanotechnol.*, 2008, **3**, 31.
- 8 G. L. Cui, L. Gu, L. J. Zhi, N. Kaskhedikar, P. A. van Aken, K. Mullen and J. Maier, *Adv. Mater.*, 2008, **20**, 3079.
- 9 C. M. Park, J. H. Kim, H. Kim and H. J. Sohn, *Chem. Soc. Rev.*, 2010, **39**, 3115.
- 10 X. W. Lou, Y. Wang, C. Yuan, J. Y. Lee and L. A. Archer, *Adv. Mater.*, 2006, **18**, 2325.
- 11 X. W. Lou, L. A. Archer and Z. C. Yang, *Adv. Mater.*, 2008, **20**, 3987.
- 12 K. T. Nam, D. W. Kim, P. J. Yoo, C. Y. Chiang, N. Meethong, P. T. Hammond, Y. M. Chiang and A. M. Belcher, *Science*, 2006, **312**, 885.
- 13 M. H. Park, K. Kim, J. Kim and J. Cho, *Adv. Mater.*, 2010, **22**, 415.
- 14 S. L. Zhu, A. C. Marschilok, E. S. Takeuchi, G. T. Yee, G. B. Wang and K. J. Takeuchi, *J. Electrochem. Soc.*, 2010, **157**, A1158.
- 15 S. L. Zhu, A. C. Marschilok, E. S. Takeuchi and K. J. Takeuchi, *Electrochem. Solid-State Lett.*, 2009, **12**, A91.
- 16 W. M. Zhang, X. L. Wu, J. S. Hu, Y. G. Guo and L. J. Wan, *Adv. Funct. Mater.*, 2008, **18**, 3941.
- 17 A. Magasinski, P. Dixon, B. Hertzberg, A. Kvit, J. Ayala and G. Yushin, *Nat. Mater.*, 2010, **9**, 353.
- 18 X. L. Ji, K. T. Lee and L. F. Nazar, *Nat. Mater.*, 2009, **8**, 500.
- 19 S. M. Paek, E. Yoo and I. Honma, *Nano Lett.*, 2009, **9**, 72.
- 20 A. L. M. Reddy, M. M. Shaijumon, S. R. Gowda and P. M. Ajayan, *Nano Lett.*, 2009, **9**, 1002.
- 21 G. Derrien, J. Hassoun, S. Panero and B. Scrosati, *Adv. Mater.*, 2007, **19**, 2336.
- 22 D. S. Su and R. Schlogl, *ChemSusChem*, 2010, **3**, 136.
- 23 X. M. Liu, Z. D. Huang, S. W. Oh, B. Zhang, P. C. Ma, M. F. Yuen and J. K. Kim, *Compos. Sci. Technol.*, 2012, **72**, 121.
- 24 A. Marschilok, C. Y. Lee, A. Subramanian, K. J. Takeuchi and E. S. Takeuchi, *Energy Environ. Sci.*, 2011, **4**, 2943.
- 25 Z. C. Yang, J. G. Shen and L. A. Archer, *J. Mater. Chem.*, 2011, **21**, 11092.
- 26 F. J. Schork, Y. W. Luo, W. Smulders, J. P. Russum, A. Butte and K. Fontenot, Miniemulsion polymerization in *Advances in Polymer Science*, M. Okubo, ed. Springer-Verlag, Heidelberg, 2005, 19–145.
- 27 R. Soula, B. Saillard, R. Spitz, J. Claverie, M. F. Llauro and C. Monnet, *Macromolecules*, 2002, **35**, 1513.
- 28 K. Min, H. F. Gao and K. Matyjaszewski, *J. Am. Chem. Soc.*, 2005, **127**, 3825.
- 29 K. Landfester, *Angew. Chem., Int. Ed.*, 2009, **48**, 4488.
- 30 E. Schreiber, U. Ziener, A. Mancke, A. Plett, P. Ziemann and K. Landfester, *Chem. Mater.*, 2009, **21**, 1750.
- 31 J. W. Choi, G. Cheruvally, H. J. Ahn, K. W. Kim and J. H. Ahn, *J. Power Sources*, 2006, **163**, 158.
- 32 D. Golodnitsky and E. Peled, *Electrochim. Acta*, 1999, **45**, 335.
- 33 S. Y. Huang, X. Y. Liu, Q. Y. Li and J. Chen, *J. Alloys Compd.*, 2009, **472**, L9.
- 34 R. Fong, C. H. W. Jones and J. R. Dahn, *J. Power Sources*, 1989, **26**, 333.
- 35 Y. Shao-Horn, S. Osmialowski and Q. C. Horn, *J. Electrochem. Soc.*, 2002, **149**, A1547.
- 36 N. Jayaprakash, J. Shen, S. S. Moganty, A. Corona and L. A. Archer, *Angew. Chem., Int. Ed.*, 2011, **50**, 5904.
- 37 M. Wachtler, J. O. Besenhard and M. Winter, *J. Power Sources*, 2001, **94**, 189.
- 38 M. Winter and J. O. Besenhard, *Electrochim. Acta*, 1999, **45**, 31.
- 39 N. Tamura, R. Ohshita, M. Fujimoto, S. Fujitani, M. Kamino and I. Yonezu, *J. Power Sources*, 2002, **107**, 48.
- 40 X. L. Wang, W. Q. Han, J. J. Chen and J. Graetz, *ACS Appl. Mater. Interfaces*, 2010, **2**, 1548.
- 41 J. Hassoun, S. Panero, P. Simon, P. L. Taberna and B. Scrosati, *Adv. Mater.*, 2007, **19**, 1632.
- 42 O. Mao, R. A. Dunlap and J. R. Dahn, *J. Electrochem. Soc.*, 1999, **146**, 405.
- 43 O. Mao and J. R. Dahn, *J. Electrochem. Soc.*, 1999, **146**, 414.
- 44 C. Q. Zhang, J. P. Tu, X. H. Huang, Y. F. Yuan, S. F. Wang and F. Mao, *J. Alloys Compd.*, 2008, **457**, 81.
- 45 C. J. Wen and R. A. Huggins, *J. Electrochem. Soc.*, 1981, **128**, 1181.
- 46 D. Larcher, C. Masquelier, D. Bonnin, Y. Chabre, V. Masson, J. B. Leriche and J. M. Tarascon, *J. Electrochem. Soc.*, 2003, **150**, A133.
- 47 M. F. Hassan, Z. P. Guo, Z. X. Chen and H. K. Liu, *Mater. Res. Bull.*, 2011, **46**, 858.
- 48 S. Hariharan, K. Saravanan and P. Balaya, *Electrochem. Solid-State Lett.*, 2010, **13**, A132.
- 49 M. M. Thackeray, W. I. F. David and J. B. Goodenough, *Mater. Res. Bull.*, 1982, **17**, 785.
- 50 J. Manuel, J. K. Kim, J. H. Ahn, G. Cheruvally, G. S. Chauhan, J. W. Choi and K. W. Kim, *J. Power Sources*, 2008, **184**, 527.